Development of an image Mean Square Displacement (iMSD)-based method as a novel approach to study the intracellular trafficking of nanoparticles

Luca Digiacomo[a,b], Michelle A. Digman[c], Enrico Gratton[c], Giulio Caracciolo[a,*]

[a] *Department of Molecular Medicine, Sapienza University of Rome, Viale Regina Elena 291, 00161 Rome, Italy*
[b] *Department of Bioscience and Biotechnology, University of Camerino, Via Gentile III da Varano, 62032 Camerino, (MC), Italy*
[c] *Laboratory for Fluorescence Dynamics, Biomedical Engineering Department, University of California at Irvine, Irvine, CA 92697, USA*

Abstract

Fluorescence microscopy and spectroscopy techniques are commonly used to investigate complex and interacting biological systems (e.g. proteins and nanoparticles in living cells), since these techniques can explore intracellular dynamics with high time resolution at the nanoscale. Here we extended one of the Image Correlation Spectroscopy (ICS) methods, i.e. the image Mean Square Displacement, in order to study 2-dimensional diffusive and flow motion in confined systems, whose driving speed is uniformly distributed in a variable angular range. Although these conditions are not deeply investigated in the current literature, they can be commonly found in the intracellular trafficking of nanocarriers, which diffuse in the cytoplasm and/or may move along the cytoskeleton in different directions. The proposed approach could reveal the underlying system's symmetry using methods derived from fluorescence correlation concepts and could recover dynamic and geometric features which are commonly done by single particle analyses. Furthermore, it improves the characterization of low-speed flow motions, when compared to SpatioTemporal Image Correlation Spectroscopy (STICS). Although we present a specific example (lipoplexes in living cells), the emphasis is in the discussion of the method, its basic assumptions and its validation on numeric simulations.

Keywords: Image Correlation Spectroscopy (ICS), intracellular trafficking, drug and gene delivery.

Statement of Significance

Recent advances in nanoparticle-based drug and gene delivery systems have pointed out the interactions at cellular and subcellular levels as key-factors for the efficiency of the adopted biomaterials. Such biochemical and biophysical interactions drive and affect the intracellular dynamics, that is commonly characterized by means of fluorescence microscopy and spectroscopy techniques. Here we present a novel Image Correlation Spectroscopy (ICS) method as a promising tool to

*Corresponding author
Email address: giulio.caracciolo@uniroma1.it (Giulio Caracciolo)

capture the intracellular behavior of nanoparticles with high resolution and low background's sensitivity. This study overcomes some of the approximations adopted so far, by decoupling the flow terms of the investigated dynamics and thus recovering ensemble's information from specific single particle behaviors. Finally, relevant implications for nanoparticle-based drug delivery are shown.

1. Introduction

One important task in biophysics concerns the characterization of motion of macromolecules in living cells. This task is generally carried out by means of fluorescence microscopy or spectroscopy techniques and provides a fundamental approach to the study of dynamics and interactions at cellular and molecular levels. These methods explore a variety of biological processes involving membrane proteins [1–4], protein-protein interactions [5], nucleic acids, lateral structure of biological membranes [6], molecular diffusion and cytoplasmatic trafficking of nanoparticles (NPs) [7–9]. NPs offer unique possibilities for overcoming cellular barriers in order to improve the delivery of various drugs and gene nanomedicines. Characterizing the intracellular mode of motion of nanocarriers is rapidly emerging as a key issue in drug delivery. In this regard, Single Particle Tracking (SPT) represents the technique-of-choice [10–15], but it is extremely time consuming. On the other side, variants of Fluorescence Correlation Spectroscopy (FCS) provide techniques by which fluorescent labeled objects can be studied at high spatial and temporal resolution, without identifying single particles. In detail, FCS measures spontaneous intensity fluctuations caused by small deviations from thermal equilibrium [16, 17]. The analysis is commonly achieved by applying temporal correlation functions, which can be coupled to spatial information, for example by means of laser scanning techniques. Image Correlation Spectroscopy (ICS) operates on image stacks and globally refers to the ensemble of simultaneously detected NPs. Average values but not their distribution are obtained by ICS, but a great amount of data can be rapidly achieved due to its high statistics. Many ICS-based methods have been developed, such as Raster Image Correlation Spectroscopy (RICS) [18], Temporal and SpatioTemporal Image Correlation Spectroscopy (TICS and STICS respectively) [1, 7, 9], Particle Image Correlation Spectroscopy (PICS) [19], image Mean Square Displacement (iMSD) [2]. Each method has its own field of application such as dynamic processes ranging from diffusion of cytosolic proteins, slower processes such as the assembly and disassembly of large multiprotein complexes to determination of spatial maps of concentrations, aggregation, and dynamics in living cells. However, all of these methods have not specifically being designed to the study two-dimensional dynamical processes driven by flow terms, which are uniformly distributed within an angular range. These conditions are biologically relevant since they characterize NPs that, in turn, controls the efficiency of drug delivery.

To fulfill this gap, here we present an ICS-based method that arises from Spatio Temporal Image Correlation Spectroscopy (STICS) and image Mean Square Displacement (iMSD) and provides a degree of spatial symmetry. Specifically, we decoupled the average flow vector from the strength of the driving speed. These aspects become relevant whether a velocity map at the intracellular level is computed or the chemical and biological interactions at the nanoscale are investigated. Furthermore, the obtained results can be coupled to information arising from pair correlation-based techniques [20], that do not require spatial averaging, but detect boundaries of confinement zones and barriers to flow. We found out that this extension of the correlation analysis over a 3-dimensional domain allows a correct NP's motion characterization for low values of flow speed, under specific conditions of symmetry. This was an unexpected result, since in these regimes of NPs speed and motion symmetry, application of STICS-based techniques does result in incorrect categorization of the

NPs mode of motion, leading to misleading interpretations. We mainly focused on the analytical method, which has been validated by numeric simulations illustrating and supporting our basic assumptions. Finally, a specific example of application is given. It involves the analysis of cationic lipid/DNA nanoparticles (lipoplexes) in Chinese Hamster Ovary cells. To date, lipoplexes are are considered to be the most promising class of organic nanoparticles for a wide variety of both in vitro and in vivo applications (e.g. cell transfection, gene silencing, gene therapy etc.). Therefore, a deeper insight on the intracellular dynamics of lipoplexes shall have a profound impact for the development of further lipid-based gene delivery materials.

2. Material and methods

2.1. Preparation of complexes and confocal microscopy experiments

The cationic lipid 3β-[N-(N,N-dimethylaminoethane)-carbamoyl]-cholesterol (DC-Chol) and the zwitterionic helper lipid dioleoylphosphatidylethanolamine (DOPE) were purchased from Avanti Polar Lipids (Alabaster, AL) and used without further purification. For the preparation of cationic liposomes, the binary lipid mixtures were first dissolved in chloroform and subsequently left to evaporate under vacuum for at least 24 h. The obtained lipid films were then hydrated with Nanopure water until a final concentration of 1 mg/ml. Sonication to clarity was needed to obtain unilamellar cationic liposomes. In order to form binary liposome/DNA complexes, 100 μl of phosphate buffered saline (PBS) were added to a 5 μl dispersion containing binary liposomes. The same amount of buffer was added to 1 μl of plasmid DNA (pDNA). The solutions were subsequently left to equilibrate for a few minutes. Then, the pDNA solution was poured in the liposome dispersion and after 20 minutes the complexes were ready to use. CHO-K1 cells were purchased from American Type Culture Collection (CCL-61 ATCC) and were grown in Hams F12K medium supplemented with 10% of Fetal Bovine Serum (FBS) at 37°C and in 5% CO_2. Confocal microscopy experiments were carried out using a Fluoview FV-1000 (Olympus, Tokyo, Japan) microscope, provided with a 543 nm HeNe laser, as excitation source. Data were collected at 37°C and were controlled by a proper acquisition software (FV10-ASW, Olympus, Tokyo, Japan).

2.2. Numeric simulations and data analysis

In silico validations have been carried out by simulating image-stacks with tunable dynamic parameters (i.e. diffusion coefficient and strength, direction and angular distribution of flow speed), total length, number and size of spot-like nanoparticles. First, a set of single particle tracks was generated according to the dynamic input arguments. Then, the trajectories were randomly distributed over a square domain, which corresponds to the image matrix. Finally, the obtained template was used to locate the Gaussian spots, frame by frame. All simulations and data analyses were performed off-line using a commercial software package (MATLAB 7.13, The MathWorks Inc., Natick, MA, 2011).

3. Theory

ICS-based techniques focus on the correlation of fluorescence fluctuations, which are computed from the intensities recorded in the image time-series, pixel by pixel, frame by frame. In detail, a generalized spatiotemporal intensity fluctuation correlation function can be defined as

$$g(\xi,\eta,\tau) = \frac{\langle \delta i(x,y,t)\, \delta i(x+\xi, y+\eta, t+\tau)\rangle}{\langle i(x,y)\rangle_t \langle i(x,y)\rangle_{t+\tau}} \tag{1}$$

where ξ, η and τ represent two spatial and a temporal lag variables, respectively and $\delta i(x,y,t)$ is the intensity fluctuation at pixel position (x,y) and time t, i.e. $\delta i(x,y,t) = i(x,y,t) - \langle i(x,y)\rangle_t$ [1]. $g(\xi,\eta,\tau)$ is typically calculated by Fourier methods and fit to standard Gaussian functions. The spatial correlation at time t can be evaluated from Eq. 1 by imposing a zero time-lag:

$$g(\xi,\eta,0)_t = \frac{\langle \delta i(x,y,t)\, \delta i(x+\xi, y+\eta, t)\rangle}{\langle i(x,y)\rangle_t^2} \tag{2}$$

Furthermore, the k-th spatial correlation function of the image-stack can be fitted by a 2-dimensional Gaussian surface of scale factor $G_{0(k)}$, offset $G_{\infty(k)}$ and variance ω_k^2:

$$g(\xi,\eta,0)_k = G_{0(k)} \exp\left\{-\frac{\xi^2+\eta^2}{\omega_k^2}\right\} + G_{\infty(k)} \tag{3}$$

Similarly, the temporal correlation function is defined by evaluating the generalized correlation function at zero spatial-lag:

$$g(0,0,\tau) = \frac{\langle \delta i(x,y,t)\, \delta i(x,y,t+\tau)\rangle}{\langle i(x,y)\rangle_t \langle i(x,y)\rangle_{t+\tau}} \tag{4}$$

Motion characterization and measurements of the dynamic parameters can be carried out by evaluating the time correlation function, i.e. by fitting $g(\xi,\eta,\tau)$ at the origin of the (ξ,η)-plane, with the following curve:

$$\begin{aligned} g(0,0,\tau) = G_\infty + G_0 \left(1+\frac{\tau}{\tau_d}\right)^{-1} \times \\ \exp\left\{-\left(\frac{\tau}{\tau_f}\right)^2 \left(1+\frac{\tau}{\tau_d}\right)^{-1}\right\} \end{aligned} \tag{5}$$

where ω is the mean correlation radius, obtained by averaging the ω_k-values, which have been measured by fitting Eq. 3 for every image in the stack. v is the modulus of the flow speed, $\tau_d = \omega/(4D)$ and $\tau_f = \omega/v$ represent the characteristic diffusion decay time and flow time, respectively [1]. Particles undergoing Brownian diffusion tend to exit the correlation area in a symmetric fashion, thus broadening the Gaussian surface in any direction [7]: the peak is then centered at $(\xi_0,\eta_0) = (0,0)$ and its value decreases with time. If a flow term $\vec{v}$ along a specific direction ϕ_0 is added to the particle dynamics, a drift contribution affects the correlation function and the Gaussian peak is subsequently shifted to the lag positions $\xi_0 = -v_x\tau = v_\xi\tau$; $\eta_0 = -v_y\tau = v_\eta\tau$. However, the fitting procedure on the temporal correlation function alone (Eq. 5) is directionally blind to the flow speed $\vec{v}$. Instead its extension over a spatiotemporal domain adds information about speed's average direction and strength, but only measures the net resultant directed component [1]. Thus, the aforementioned approaches yield different velocity values when particles uniformly flow within a non-zero angular range.

This condition can be described as a system of M particles undergoing Brownian diffusion and driven by a flow motion of speed $\vec{v}_k$ $(k = 1, 2 \ldots M)$, which is uniformly distributed around a fixed direction ϕ_0, within an angular range ψ. Hence, ϕ_0 is responsible for the problem's anisotropy and ψ defines the system's symmetry. As an instance, Figure 1 shows some representative sets of trajectories, whose flow speed is centered at $\phi_0 = \pi/4$, for different ψ-values. In order to decouple

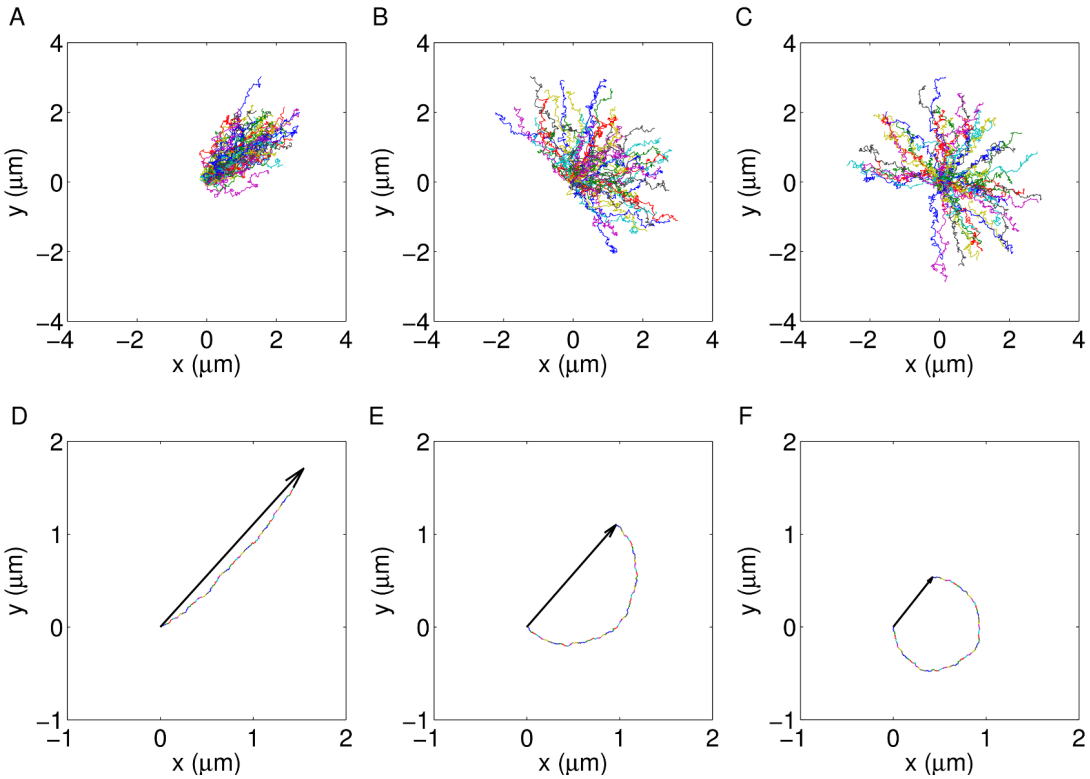

Figure 1: (A, B, C) Sets of 50 tracks and (D, E, F) corresponding average displacements from the origin, for dynamics driven by Brownian diffusion + uniformly distributed flow motion ($D = 0.75\,10^{-3}\,\mu\text{m}^2\ \text{s}^{-1}$; $v = 1.5\,10^{-2}\,\mu\text{m}\ \text{s}^{-1}$; $\phi_0 = \pi/4$ and $\psi_A = \pi/6$, $\psi_B = \pi$, $\psi_C = 3\pi/2$).

the flow's effects on the correlation function and take into account the symmetry properties arising from the angular distribution of the driving speed, we adopted and extended the image-Mean Square Displacement (i-MSD) method. The theory of iMSD has been developed and validated for Brownian and confined diffusions to describe the protein lateral motion in cell membranes [2]. It starts from the following expression of $g(\xi, \eta, \tau)$:

$$g(\xi, \eta, \tau) = g_0\, p(\xi, \eta, \tau) \otimes W(\xi, \eta) \tag{6}$$

where g_0 defines the contrast of fluctuation and is related to the average number of particles in the observation volume, $W(\xi, \eta)$ is known as the instrument Point Spread Function (PSF) and $p(\xi, \eta, \tau)$ is the probability function describing the dispersive dynamics. Its expression is strictly related to the single particle's transition probability $P(\vec{r}\,'|\vec{r}, \tau)$, i.e. the probability that a particle originally at $\vec{r}$, will be at $\vec{r}\,'$ after a time period τ. For Brownian diffusion + directed motion it reads [14, 21]

$$P(\vec{r}\,'|\vec{r}, \tau) = \frac{1}{4\pi D\tau} \exp\left\{-\frac{|\vec{r}\,' - \vec{r} - \vec{v}\tau|^2}{4D\tau}\right\} \tag{7}$$

The spatiotemporal correlation gives overall information about the entire set of the investigated particles. Thus, it involves an ensemble average of the single particle behaviors and it is affected by the spatial distribution of the flow terms. Brownian diffusion yields linear trends of the correlation Gaussian's variance [2], ordered fluxes are responsible for the peak's shift [7] and the system's symmetry contributes to a further (anisotropic) spread of the correlation function. For $\tau \ll \tau_f$, $g(\xi, \eta, \tau)$ can be approximated by the following relationship:

$$g(\xi,\eta,\tau) = G_\infty + G_1(\tau) \times \exp\left\{-\frac{[\xi - v_\xi\,\tau]^2 + [\eta - v_\eta\,\tau]^2}{\sigma^2(\tau)}\right\} \tag{8}$$

where

$$v_\phi = (v_\xi^2 + v_\eta^2)^{\frac{1}{2}} = a_\phi v < v \tag{9}$$

and

$$\vec{v}_\phi = -\langle\vec{v}\rangle \tag{10}$$

The negative sign arises from the fact that the Gaussian correlation peak moves in a direction opposite to the flow. Therefore, the flow contribution to the peak's shift can be quantified by the a_ϕ-parameter, which is related to the system's symmetry, varies from 0 ($\psi = 2\pi \Rightarrow \langle\vec{v}\rangle = 0$) to 1 ($\psi = 0 \Rightarrow \langle\vec{v}\rangle = v$) and reads (Eq. 9)

$$a_\phi^2 = \frac{\langle\vec{v}\rangle^2}{\langle v^2\rangle} \tag{11}$$

In order to explore the drift contribution over the entire domain ($0 < \psi < 2\pi$), we can first express the position of the k-th particle at time t as $\vec{r}_k = \vec{v}_k t$. This corresponds to neglecting the effect of the diffusion over the spatial distribution of the particle position. Under this assumption, after a time period t every particle will be at a distance $|\vec{r}(t)|$ from its starting position and

$$a_\phi^2 = \frac{\langle\vec{r}(t)\rangle^2}{\langle r^2(t)\rangle} \tag{12}$$

Furthermore, $\langle\vec{r}(t)\rangle$ can be analytically related to the angular dispersion ψ. Indeed, by choosing a reference axis along the ϕ-direction, it reads

$$\langle\vec{r}\rangle = \frac{\int_0^{\psi/2} |\vec{r}|\cos\theta d\theta}{\int_0^{\psi/2} d\theta} = \frac{2}{\psi}\sin\left(\frac{\psi}{2}\right)|\vec{r}| \tag{13}$$

and finally

$$a_\phi^2 = \left[\frac{2}{\psi}\sin\left(\frac{\psi}{2}\right)\right]^2 \tag{14}$$

Hence, the correlation function moves in the ϕ-direction with a decreasing drift with respect to the particle speed angular dispersion. This argument leads to the definition of another flow contribution, which is not detectable from the peak's shift, but is complementary to a_ϕ^2. It can be written as

$$a_\sigma^2 = 1 - a_\phi^2 = \frac{\langle r^2(t)\rangle - \langle\vec{r}(t)\rangle^2}{\langle r^2(t)\rangle} = \frac{\langle[\vec{r}(t) - \langle\vec{r}(t)\rangle]^2\rangle}{\langle r^2(t)\rangle} \tag{15}$$

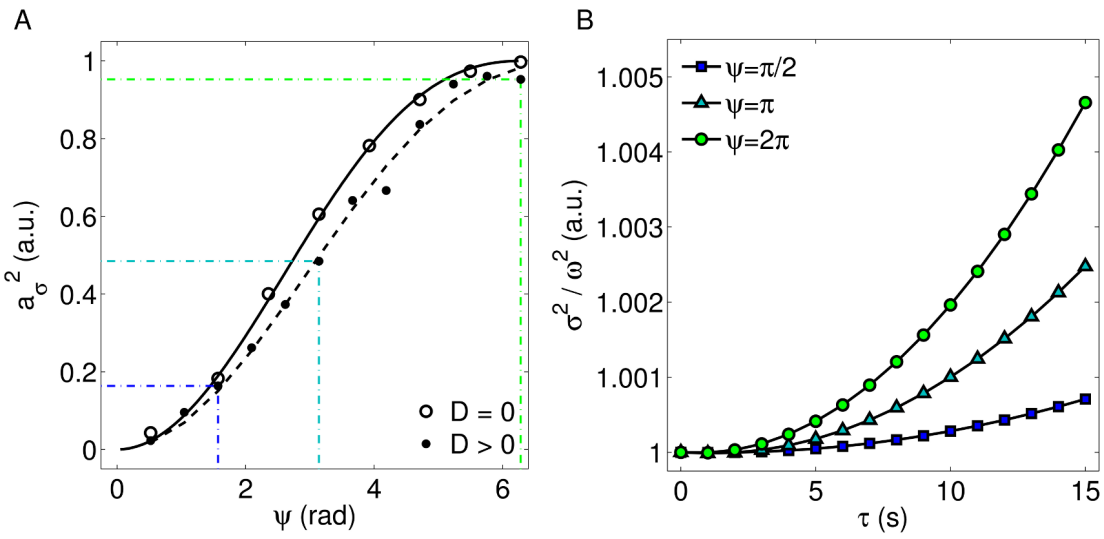

Figure 2: (A) Symmetry parameter a_σ^2 as function of ψ for strongly directed motion and diffusive + flow motion ($D = 0.75\,10^{-3}\,\mu\text{m}^2\ \text{s}^{-1}$; $v = 0.5\,10^{-2}\,\mu\text{m s}^{-1}$). (B) Corresponding Gaussian's variance for three different ψ-values.

and it is involved in the time evolution of the fitting Gaussian's variance (i.e. $\sigma^2(\tau)$ in Eq. 8). On the other hand, the numerator in Eq. 15 is the second central moment of $\vec{r}$, i.e. the mean square displacement over the ensemble, at time t. Flow motions add a quadratic term to $\sigma^2(\tau)$, that is related to the complementary contribution a_σ^2. In other words

$$\sigma^2(\tau) = \omega^2 + 4D\tau + v_\sigma^2\tau^2 \tag{16}$$

where

$$v_\sigma^2 = a_\sigma^2 v^2 \tag{17}$$

Therefore, the parabolic term increases with the system's symmetry (Fig. 2) and v can be finally calculated as

$$v^2 = v_\phi^2 + v_\sigma^2 = (a_\phi^2 + a_\sigma^2)v^2 \tag{18}$$

The effect of the Brownian diffusion over the symmetry parameters is a deviation from the functional relationship 14 (Fig. 2). This deviation is such that a_ϕ follows the trend of a specific single track asphericity. It is evaluated over the trajectory which is obtained by translating all the tracks of the ensemble, one after the other. Therefore, the asphericity is an ensemble's parameter arising from single particle analyses. It is defined from the gyration tensor of the particle trajectories [22, 23] and quantifies the mean square displacement of the particle positions along two orthogonal directions.

4. Results and discussion

4.1. Dynamic parameters and system's symmetry

In order to validate the proposed method, tests on numerical simulation have been carried out. In this section we present some representative examples mimicking the dynamics of nanoparticle

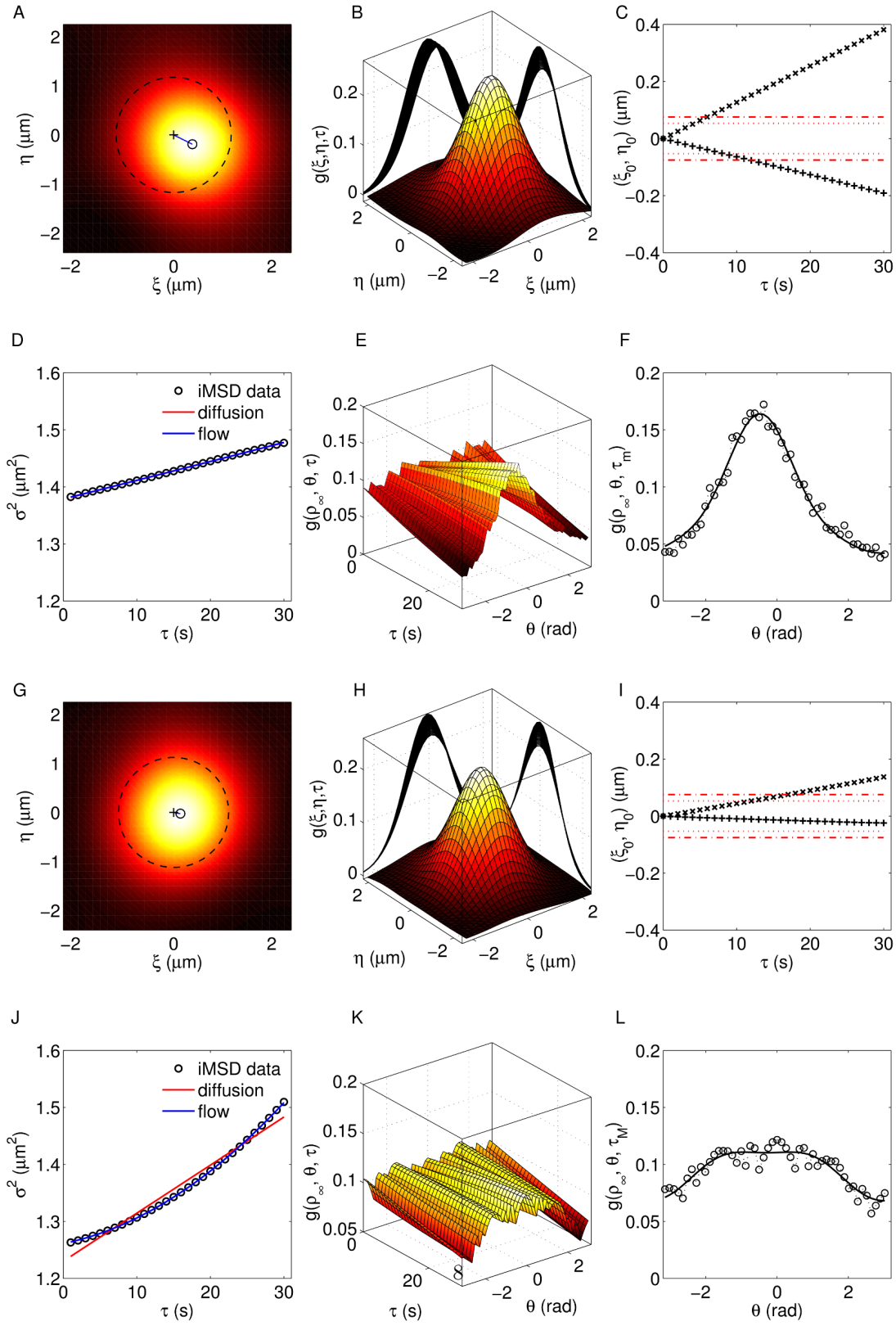

Figure 3: iMSD analysis of two representative conditions with same dynamic parameters ($D = 0.75\,10^{-3}\,\mu\text{m}^2\ \text{s}^{-1}$; $v = 1.5\,10^{-2}\,\mu\text{m}\ \text{s}^{-1}$; $\phi = -\pi/6$) and different angular dispersions $\psi_1 = \pi/4$ (top panles), $\psi_2 = 3\pi/2$ (bottom panels). (A, G) Top view and (B, H) 3D view of the correlation function, (C, I) peak's position as function of time ("×" for $\xi_0(\tau)$, "+" for $\eta_0(\tau)$), (D, J) time evolution of σ^2 from $\tau = 0$ to $\tau = \tau_m = 30\,\text{s}$ and (E, F, K, L) circular sections $g(\rho_\infty, \theta, \tau)$, $g(\rho_\infty, \theta, \tau_m)$ for $\rho_\infty = \omega$.

inside the cytoplasm. They consist on image-stacks of length $N = 300$ frames, size 256×256 px^2, containing $M = 50$ spots undergoing Brownian diffusion ($D = 0.75\,10^{-3}\,\mu$m^2 s^{-1}) + flow motion ($v = 1.5\,10^{-2}\,\mu$m s^{-1}) and different angular dispersion (Fig 3). For low ψ-values (e.g. $\psi = \pi/4$, top panels) the shift of the fitting surface is manifest and it can be measured through the centroid's position $(\xi_0(\tau), \eta_0(\tau))$ (Fig. 3C). Conversely, the parabolic contribution of the Gaussian's variance is very small (Fig. 3D). Finally, the angular distribution $g(\rho_\infty, \theta, \tau)$ presents a peak centered at $\theta = \phi$ (Fig. 3 panels E, F). On the other side, high ψ-values (e.g. $\psi = 3\pi/2$) yield lower shifts of the correlation function, corresponding to flatter angular distribution and remarkable quadratic contribution to the time evolution of σ^2 (Fig. 3, bottom panels). The intermediate conditions of symmetry can be explored by varying ψ (Fig. 4). As expected, high drift contribution corresponds to low quadratic terms in the variance curve, which approaches to linear trends for $\psi \to 0$. On the other hand, increasing ψ yields lower shifts and higher parabolic terms. Furthermore, the angular distribution's peak is centered at ϕ and the intercept of $\sigma^2(\tau)$ is equal to the measured ω^2, for any ψ-value. Finally, we measured the symmetry parameter a_σ^2, the diffusion coefficient D and the flow speed v, as functions of ψ. As expected, a slight underestimation of a_σ^2 with respect to the ideal curve ($D = 0$) has been found out. This trend is confirmed by the measurements of the dynamic parameters, whose percentage deviations with respect to the input arguments are lower than 15% for D and 5% for v.

4.2. Detection of low-speed flow motion

The lowest value of flow speed, which can be detected at a given diffusion coefficient, depends on the experimental set up (through ω, pixel size and total period of acquisition) and on the system itself (through D, v and ψ). As an instance, particles directed with small angular dispersion and low flow speed (with respect to the diffusion coefficient) yield a detectable drift at high τ, which can be out of the measurement range. Instead, if the symmetric contribution is dominant, the measurement of v is based on the parabolic term of σ^2, which can be imperceptible within the observation time scale at a given ω. Under low-speed conditions, the analysis of the correlation function over the (ξ, η)-plane improves the STICS motion characterization. Indeed, finite values of ω can yield a negligible flow contribution to $g(0, 0, \tau)$, whose trend results indistinguishable from the diffusive one. On the other side, the iMSD approach detects flow effects on the Gaussian variance or the peak's shift. Fig. 5 shows a representative example, obtained by simulating dynamics mainly governed by Brownian diffusion, with a small speed term, for different angular dispersions. It is found out that there exists a critical value ψ_c, such that STICS does not distinguish flow terms for $\psi < \psi_c$. However, the characterization of motion is successfully carried out trough iMSD, which discriminats the kind of dynamics for any ψ, even if the measured parameters are underestimated. Of note, no thresholds are needed to carry out the analysis. More precisely, all the diffusive trends are included in the general forms of the functional relationships and can be obtained from them if $v \to 0$. The fitting computation is carried out through the general forms 5, 16 and yields redundant flow terms if the dynamic is driven only by diffusion. In other words, the measured v-values are close to 0 and the fitting error $\delta(v)$ are very high, thus resulting in $\delta(v)/v \to \infty$. Instead, dynamics governed by Brownian diffusion + flow motion present finite values of v, $\delta(v)/v$ and higher fitting determination coefficient R^2, with respect to the simple diffusive models.

The detection limits are therefore dictated only by the adopted experimental conditions and the investigated system. Indeed, the spatial average involved in the correlation ultimately determines the spatial resolution of the method and the minimum time delay of the experimental apparatus determines the behavior at very short time. Furthermore, the ability in discriminating Brownian

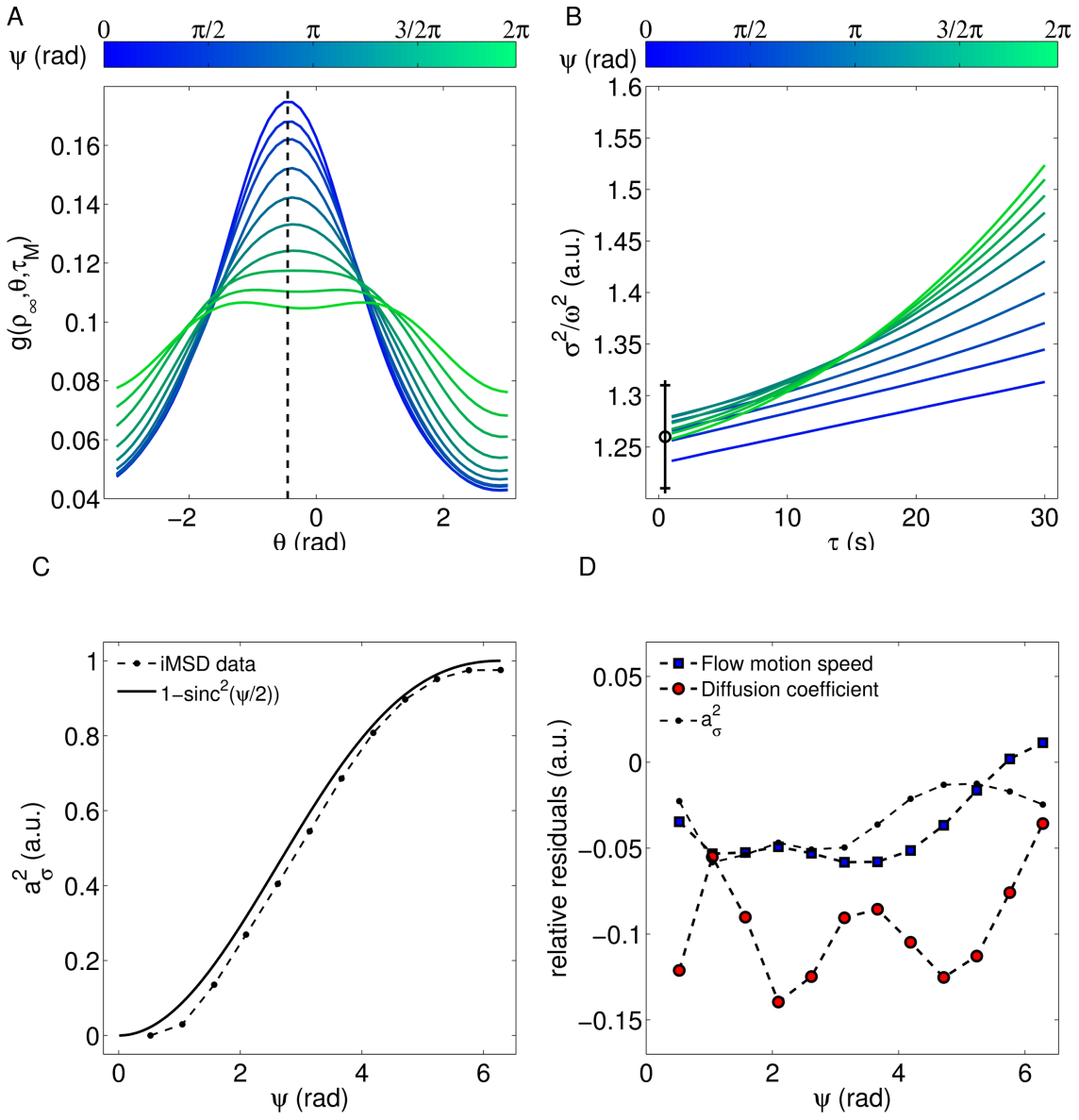

Figure 4: (A) Circular section of the correlation function at $\rho_\infty = \omega$, $\tau = \tau_m$, for dynamics driven by same flow speed v and different angular dispersions ψ. Remarkable drift's effects are manifest for low ψ-values. (B) Corresponding time evolution of σ^2, The parabolic contribution increases with ψ, complementarily to the peak's shift. The black errorbar shows the square correlation radius, measured through Eq. 3. (C) Measured symmetry coefficient a_σ^2 and (D) relative residuals from the expected values of the dynamic parameters, as functions of ψ. Input arguments: $D = 0.75\,10^{-3}\,\mu\text{m}^2\ \text{s}^{-1}$; $v = 1.5\,10^{-2}\,\mu\text{m}\ \text{s}^{-1}$; $\phi = -\pi/6$.

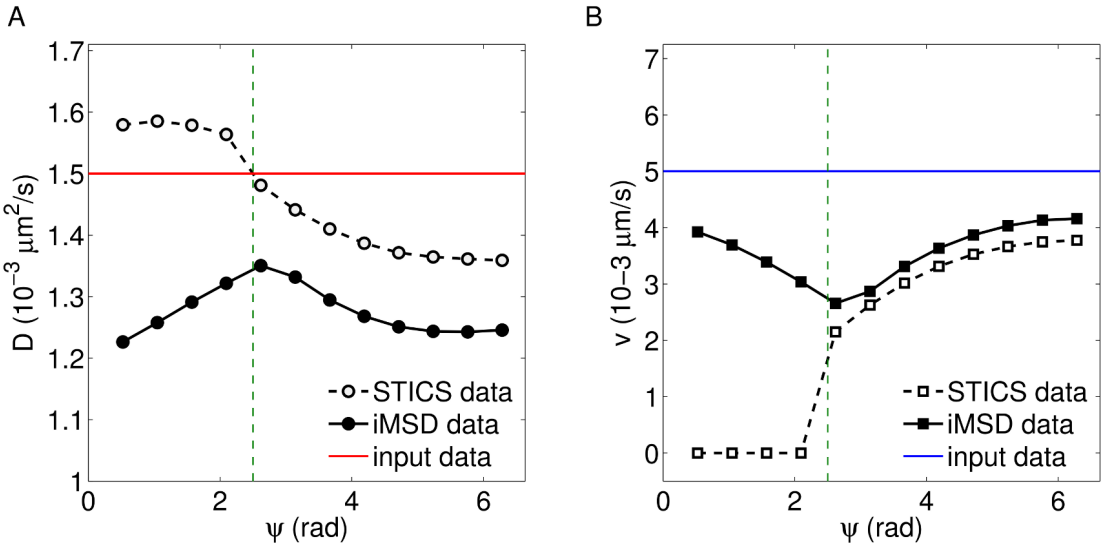

Figure 5: (A) Measured diffusion coefficient and (B) flow speed as functions of ψ, obtained from STICS and iMSD. The vertical lines individuate ψ_c, the input parameters are shown as horizontal red and blue lines, respectively for $D = 1.5\,10^{-3}\,\mu\text{m}^2\ \text{s}^{-1}$ and $v = 0.5\,10^{-2}\,\mu\text{m}\ \text{s}^{-1}$.

diffusions from flows involves the correlation radius, which is related to the geometry of laser beam and the finite dimensions of spots. Therefore, although the discussion has been focused on slow dynamics mimicking the cytoplasmatic trafficking of nanoparticles, other biophysical systems can be studied through the proposed approach, with a preliminary optimization of the experimental and analytical parameters (i.e. minimum time delay, total length of image-stacks, maximum time-lag for correlation, pixel size, extension of the fitting domain).

4.3. Background's effects

In the experiments the spatiotemporal correlation function is generally affected by changes of the overall background within the region of calculation, in which case it is difficult to discriminate the contribution of particles. Here, we discuss the effects of slowly changing background on the measurement of the dynamic parameters. This argument is based on the analyses of simulations and the comparison of results obtained from STICS and iMSD approaches. In order to mimic the actual conditions of acquisition, a Gaussian noise of tunable strength and a sinusoid function of random phase and temporal period T_b are added to the simulated signals, pixel by pixel. Thus, the resulting image-stack contains moving spots over a varying background (Fig. 6 panels A and B). The proportion between the intensities of spots and background defines the signal-to-noise ratio and the intensity distribution quantifies the number of pixels with intensity within the range $(i, i + \Delta i)$. Common procedures of background removal act on the intensity distribution and filter the signals which overcome a tunable threshold value.

The temporal correlation function is affected by the background (Fig. 6D), since it varies over times and modulates the correlation at zero spatial-lag. The oscillations of $g(0, 0, \tau)$ depend on T_b

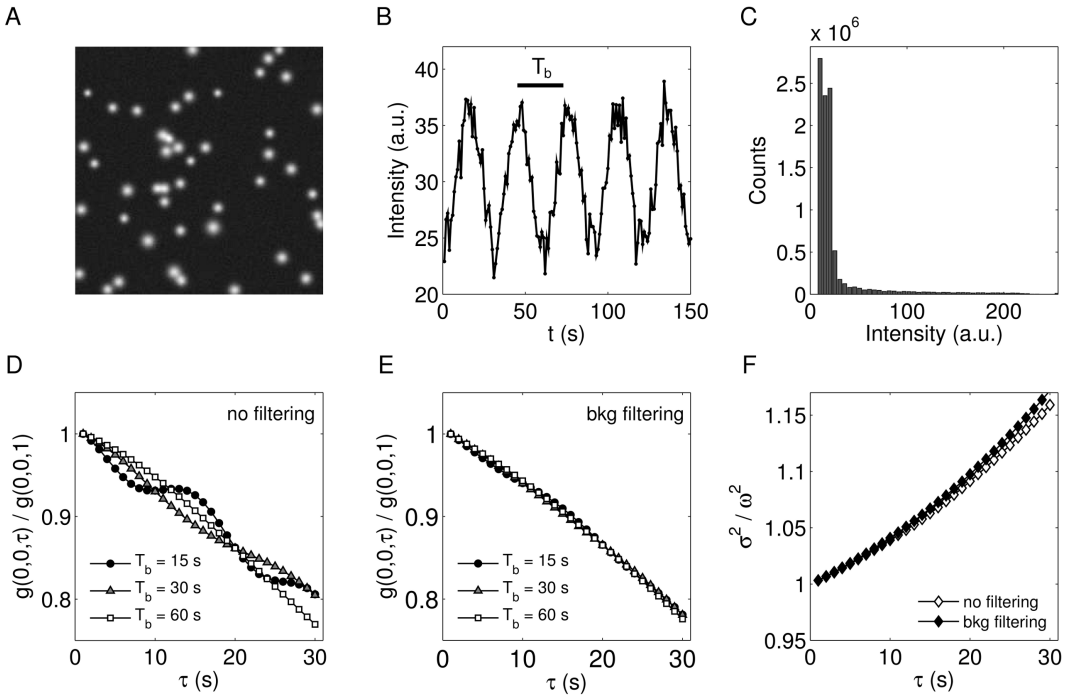

Figure 6: (A) First frame of a simulated image-stack affected by slowly changing background. (B) Background intensity as a function of time: a Gaussian noise is added to a modulating sinusoid function of period T_b. (C) Intensity distribution over the image-stack, adopted to set the background filter. (D) Effects of background on the temporal correlation function and (E) corresponding curves after the filtering procedure. (F) Background's effect on the Gaussian's variance ($T_b = 30\,\mathrm{s}$). The presented dynamics is characterized by the following input parameters: $D = 10^{-3}\,\mu\mathrm{m}^2\ \mathrm{s}^{-1}$; $v = 1.5\,10^{-2}\,\mu\mathrm{m\ s}^{-1}$; $\psi = \pi$; $\phi = \pi/6$.

	STICS		iMSD	
$T_b(s)$	ΔD (%)	Δv (%)	ΔD (%)	Δv (%)
1	17.7	-8.18	-6.80	-7.75
5	47.2	11.1	-6.89	-7.75
10	39.8	-2.75	-6.91	-7.75
15	37.0	-11.9	-6.60	-7.81
20	20.4	-7.93	-9.21	-7.75
30	71.3	-17.0	-6.12	-7.81
60	55.1	-2.43	-6.10	-6.07

Table 1: STICS and iMSD measurement of the dynamic parameters after the background removal. Results are shown as percentage differences from the input data.

and alter the measurements of the dynamic parameters. However, the effect is reduced when the background is removed from the original image-stack (Fig. 6E). On the other side, the background

	D ($10^{-3}\mu$m^{2}s^{-1})	v ($10^{-3}\mu$m s^{-1})	ϕ_0 (rad)	a_σ^2 (a.u.)
256×256 pixels	1.06 ± 0.16	4.64 ± 0.15	-	1.00
ROI a	1.05 ± 0.23	1.27 ± 0.04	0.10	0.00
ROI b	0.60 ± 0.26	6.30 ± 0.11	-0.55	0.00
ROI c	1.16 ± 0.11	6.86 ± 0.37	2.36	0.89

Table 2: Measurement of the dynamic parameters which define the velocity map of the presented example.

changes with no spatial periodicity and its fluctuation weakly affects the correlation over the entire (ξ, η)-plane. Subsequently, the peak's shift (not shown) and the time evolution of the Gaussian's variance (Fig. 6F) provide better estimations of the dynamic parameters. Of note, the background removal is necessary to the STICS analysis, but slightly improves iMSD measurements. Thus, the iMSD method is more stable and less sensitive to slowly changing background and its fluctuations. As an instance, we found out this general trend for different value of T_b, at a fixed signal-to-noise ratio of SNR=8.5. Tab. 1 shows the results obtained through STICS and iMSD analyses on filtered images. The dynamics is driven by $D = 10^{-3}\,\mu$m^{2}s^{-1}, $v = 1.5\,10^{-2}\,\mu$m s^{-1}, at an angular dispersion $\psi = \pi$.

4.4. Velocity map of lipid-based nanocarriers in living cells

As an example of application of the proposed method, we present the analysis of an image-stack exploring the intracellular dynamics of lipid/DNA complexes in Chinese Hamster Ovary (CHO) cells (Fig. 7A). In the proposed example, the pixel size is equal to 0.295 μm and the frame acquisition time is $\Delta t = 5$s (due to the slow dynamics of the complexes). The computation of the correlation function and the characterization of motion are carried out over the entire 256 × 256 pixels image and on three regions of interest (ROIs) of 128 × 128 pixels (Fig. 7B). The speed's contributions (v_ϕ and v_σ) are independently calculated by fitting the peak's shift $(\xi_0(\tau), \eta_0(\tau))$ and the Gaussian's variance σ^2 (Fig. 7 panels C, D). Thus, a velocity map is obtained, in terms of speed modulus ($\langle|\vec{v}|\rangle$) and average drift ($\vec{v}_\phi = \langle\vec{v}\rangle$). The analysis over the 256 × 256 pixels image does not reveal a peak's shift ($a_\phi^2 = 0$, $a_\sigma^2 = 1$), but detects a parabolic trend of σ^2. Therefore, the dynamics is characterized by flowing particles with symmetrically distributed velocities and both the diffusion coefficient and the flow speed are measured by fitting $\sigma^2(\tau)$. Conversely, uniform motions of the correlation peaks are detected for *ROI a* and *ROI b*. However, no quadratic terms affect the Gaussian's variances, thus resulting in $a_\phi^2 = 1$; $a_\sigma^2 = 0$. The corresponding dynamics are governed by Brownian diffusion + flow motion with negligible angular dispersion and differ for the values of D and v (Tab. 2). *ROI c* represents an intermediate condition: a small drift and a remarkable quadratic term are detected. Subsequently, both the anisotropic and the symmetric contributions are included to characterize the motion and measure the dynamic parameters. Tab. 2 summarizes the results. Incidentally, the information arising from the decoupled flow terms provides a deeper understanding, which can not be in general obtained by the STICS method. Furthermore, the iMSD approach is closer to the single particle analyses, since it explores both the strength of the dynamic parameters and the geometrical features of the investigated systems.

5. Conclusions

Through Image Correlation Spectroscopy, dynamic information about the investigated systems can be obtained by directly analyzing image time series and without exploring single particle be-

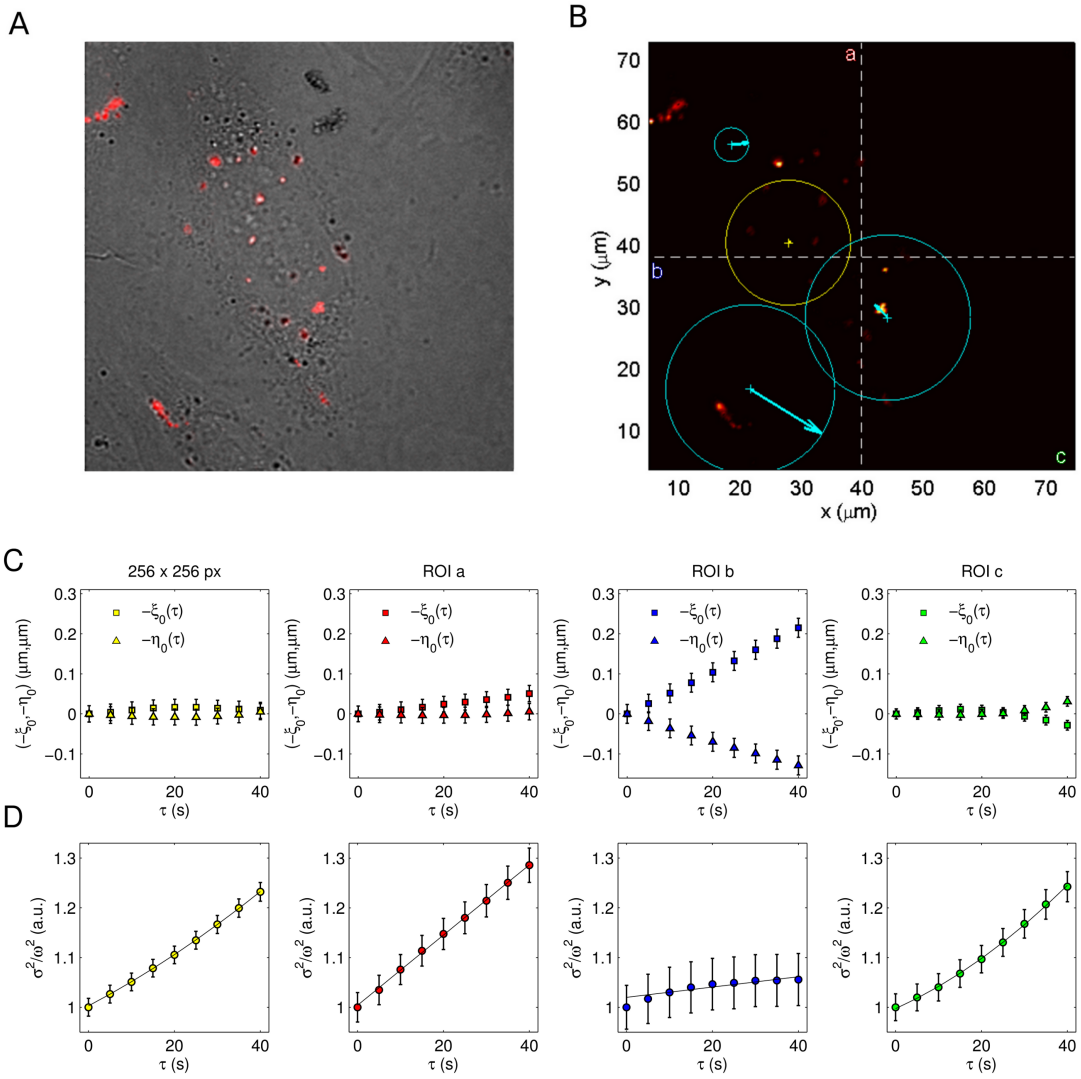

Figure 7: (A) fluorescence-labeled cationic liposomes/DNA complexes in CHO cells. (B) Velocity maps over the entire image (yellow) and on single ROIs (cyan). The arrows indicate direction and modulus of the drift's speed $\vec{v}_\phi$ and the circumferences have radius proportional to the speed modulus v. Origin of flow vectors are placed on the corresponding image center of mass. iMSD results are reported as peak's shift (C) and time evolution of Gaussian's variance (D). Both anisotropic and symmetric terms contribute to the characterization of motion.

haviors. Diffusion coefficients and flow speeds are measured by fitting procedure, acting on the spatiotemporal correlation function and defined over a domain which is included in the 3-dimensional

lag-variable space. The iMSD approach allowed us to determine the system's dynamic parameters and recover geometrical features about particles undergoing Brownian diffusion and flow motion, uniformly distributed within an angular range. This condition is a good approximation of the intracellular dynamics of gene delivery vectors, which generally diffuse in the cytoplasm and can be directed along microtubules, i.e. along manifold and different directions. By decoupling the speed spatial distribution's effects on the detected intensity fluctuations, symmetry properties and average particle drift can be evaluated. These are strictly interconnected and represent the global information arising from the motion of single particles. More precisely, if we are interested on the average particle behavior (e.g. to compute a velocity map), only the peak's drift should be take into account. Instead, biochemical properties which are responsible for the flow motion (e.g. the nanoparticle chemical affinity with the cytoskeleton), do not depend on specific directions and can be studied through the modulus of the flow speed. Furthermore, this method improves the motion characterization, especially when the diffusive contribution is dominant with respect to the flow. Indeed, when compared to the STICS approach, the study of the correlation function over the entire spatial lag-variable domain better characterize low-speed flow motion (under reasonable experimental conditions). Finally, stability in the measurement procedure and low sensitivity to slowly changing background have been demonstrated, resulting in good discrimination of the contribution of particles under realistic experimental conditions.

Acknowledgement

Dr. Daniela Pozzi is gratefully acknowledged for performing confocal microscopy experiments.

References

[1] B. Hebert, S. Costantino, P. W. Wiseman, Spatiotemporal image correlation spectroscopy (stics) theory, verification, and application to protein velocity mapping in living cho cells, Biophys. J. 88 (2005) 3601–3614.

[2] C. Di Rienzo, V. Piazza, E. Gratton, F. Beltram, F. Cardarelli, Probing short-range protein brownian motion in the cytoplasm of living cells, Nat. Commun. 5 (2014).

[3] E. Keating, A. Nohe, N. O. Petersen, Studies of distribution, location and dynamic properties of egfr on the cell surface measured by image correlation spectroscopy, Eur. Biophys. J. 37 (2008) 469–481.

[4] C. M. Brown, N. O. Petersen, An image correlation analysis of the distribution of clathrin associated adaptor protein (ap-2) at the plasma membrane, J. Cell Sci. 111 (1998) 271–281.

[5] T. Kogure, S. Karasawa, T. Araki, K. Saito, M. Kinjo, A. Miyawaki, A fluorescent variant of a protein from the stony coral montipora facilitates dual-color single-laser fluorescence cross-correlation spectroscopy, Nat. Biotechnol. 24 (2006) 577–581.

[6] S. Chiantia, J. Ries, P. Schwille, Fluorescence correlation spectroscopy in membrane structure elucidation, Biochim. Biophys. Acta-Biomembranes 1788 (2009) 225–233.

[7] S. Coppola, D. Pozzi, S. C. De Sanctis, M. Digman, E. Gratton, G. Caracciolo, Quantitative measurement of intracellular transport of nanocarriers by spatio-temporal image correlation spectroscopy, Methods Appl. Fluoresc. 1 (2013) 015005.

[8] S. Coppola, G. Caracciolo, T. Schmidt, Exact occupation probabilities for intermittent transport and application to image correlation spectroscopy, New J. Phys. 16 (2014) 113057.

[9] R. P. Kulkarni, D. D. Wu, M. E. Davis, S. E. Fraser, Quantitating intracellular transport of polyplexes by spatio-temporal image correlation spectroscopy, Proc. Natl. Acad. Sci. USA 102 (2005) 7523–7528.

[10] E. Zagato, K. Forier, T. Martens, K. Neyts, J. Demeester, S. D. Smedt, K. Remaut, K. Braeckmans, Single-particle tracking for studying nanomaterial dynamics: applications and fundamentals in drug delivery, Nanomedicine 9 (2014) 913–927.

[11] K. Remaut, V. Oorschot, K. Braeckmans, J. Klumperman, S. C. De Smedt, Lysosomal capturing of cytoplasmic injected nanoparticles by autophagy: An additional barrier to non viral gene delivery, J. Control. Release 195 (2014) 29–36.

[12] A. Sauer, K. De Bruin, N. Ruthardt, O. Mykhaylyk, C. Plank, C. Bräuchle, Dynamics of magnetic lipoplexes studied by single particle tracking in living cells, J. Control. Release 137 (2009) 136–145.

[13] H. Akita, K. Enoto, T. Masuda, H. Mizuguchi, T. Tani, H. Harashima, Particle tracking of intracellular trafficking of octaarginine-modified liposomes: a comparative study with adenovirus, Mol. Ther. 18 (2010) 955–964.

[14] H. Qian, M. P. Sheetz, E. L. Elson, Single particle tracking. analysis of diffusion and flow in two-dimensional systems., Biophys. J. 60 (1991) 910.

[15] X. Michalet, Mean square displacement analysis of single-particle trajectories with localization error: Brownian motion in an isotropic medium, Phys. Rev. E 82 (2010) 041914.

[16] E. L. Elson, D. Magde, Fluorescence correlation spectroscopy. i. conceptual basis and theory, Biopolymers 13 (1974) 1–27.

[17] J. D. C. J. Colin E. Webb, Handbook of laser technology and applications, volume 3: application, Philadelphia, Institute of Physics, 2004.

[18] M. J. Rossow, J. M. Sasaki, M. A. Digman, E. Gratton, Raster image correlation spectroscopy in live cells, Nat. Protoc. 5 (2010) 1761–1774.

[19] S. Semrau, T. Schmidt, Particle image correlation spectroscopy (pics): retrieving nanometer-scale correlations from high-density single-molecule position data, Biophys. J. 92 (2007) 613–621.

[20] M. A. Digman, E. Gratton, Imaging barriers to diffusion by pair correlation functions, Biophys. J. 97 (2009) 665–673.

[21] S. Chandrasekhar, Stochastic problems in physics and astronomy, Rev. Mod. Phys. 15 (1943) 1.

[22] J. Rudnick, G. Gaspari, The aspherity of random walks, J. Phys. A 19 (1986) L191.

[23] S. Coppola, L. C. Estrada, M. A. Digman, D. Pozzi, F. Cardarelli, E. Gratton, G. Caracciolo, Intracellular trafficking of cationic liposome–dna complexes in living cells, Soft matter 8 (2012) 7919–7927.